Half-Metallic Ferromagnetism *via* the Interface Electronic Reconstruction in $LaAlO_3/SrMnO_3$ Nanosheet Superlattices

Fang Hou,[†,‡] Tian-Yi Cai,[†] Sheng Ju,[†,*] and Ming-Rong Shen[†,*]

[†]Department of Physics and Jiangsu Key Laboratory of Thin Films, Soochow University, Suzhou 215006, P. R. China, and [‡] School of Mathematics and Physics, Suzhou University of Science and Technology, Suzhou 215009, P. R. China

ABSTRACT

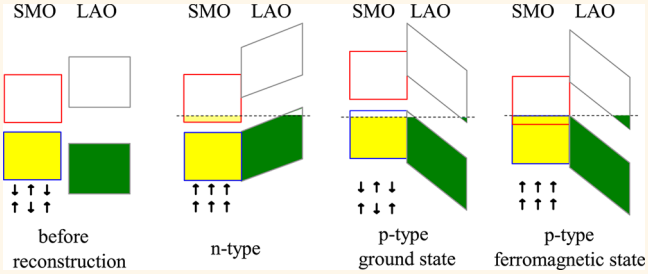

Spintronic devices are very important for future information technology. Suitable materials for such devices should have half-metallic properties with only one spin channel conducting. Nanostructures have played an important role in this aspect. Here, we report the realization of robust half-metallic ferromagnetism *via* the interface electronic reconstruction in artificial $LaAlO_3/SrMnO_3$ nanosheet supperlattices. On the basis of first-principles density-functional calculations, we reveal an obvious electron transfer from the $(LaO)^+$ layer to the adjacent $(MnO_2)^0$ layer. And the partially occupied e_g orbitals at the Mn sites can mediate a half-metallic state *via* a Zener double-exchange mechanism. On the other hand, for the superlattices with a $(SrO)^0/(AlO_2)^-$ interface, hole transfer at the interface is identified. These transferred holes reside mainly at oxygen sites in $SrMnO_3$, leading to either the preserved G-type AFM ordering in *pp*-type superlattices or complex magnetic ordering in *np*-type superlattices. Interestingly, when these systems transit to ferromagnetic ordering by an external magnetic field, an obvious change of electronic state at the Fermi level is found, suggesting a large magnetoresistive effect therein. Our studies demonstrate the unique electric and magnetic properties arising from a magnetic ordering dependent charge transfer and electronic reconstruction at perovskite heterointerfaces, and their potential applications in spintronic devices.

KEYWORDS: half-metal · nanosheet superlattice · charge transfer · electronic reconstruction · first-principles

Spintronics is based on the spin degree of freedom of the electron. Either adding the spin degree of freedom to conventional charge-based electronic devices or using the spin alone has the potential advantages of nonvolatility, increased data processing speed, decreased electric power consumption, and increased integration densities compared with conventional semiconductor devices.[1−4] Half-metallic ferromagnets, which possess the nature of a semiconductor for one spin channel and metal for another, have been the promising materials for the applications of spintronics.[5] Conventional transition metal oxide, including CrO_2 (with a Curie temperature T_C of 390 K), $La_{0.7}Sr_{0.3}MnO_3$ (T_C = 370 K), Fe_3O_4 (T_C = 860 K), and Sr_2FeMoO_6 (T_C = 400 K), have been revealed to possess highly spin-polarized electrons at the Fermi level and were studied extensively.[5] A half-metallic electronic state has also been observed in some nanostructures such as one-dimensional (1D) graphene nanoribbon,[6] 1D organometallic sandwich molecular wires,[7] and two-dimensional (2D) phthalocyanine-based organometallic single sheet.[8] However, compared with the conventional transition metal oxides, these carbon-based nanostructures show weak half-metallicity, that is, low Curie temperature and small exchange splitting energy, therefore preventing them from room-temperature application.

Recent progress in the fabrication of an atomic nanoscale multilayer superlattice opens exciting opportunities in the design of materials with emergent phenomena.[9−11] In particular, interfaces between oxide nanosheets display unexpected properties. For example, an electronic reconstruction effect leads to a two-dimensional metallic state at the interface between a band insulator $SrTiO_3$ and a Mott insulator $LaTiO_3$, as well as the interface between two band insulators of $SrTiO_3$ and $LaAlO_3$.[12−16] The basic physics lies at the charge discontinuity at the heterointerface and consequently electronic reconstruction *via* polar-field-driven charge transfer from the $(LaO)^+$ plane to the adjacent $(TiO_2)^0$ plane, making Ti 3d empty orbitals partially occupied and 2D electron gas.[17] Unlike metal-dielectric heterostructures,[18−20] the development of ferromagnetic (FM) ordering, however, is not straightforward in

* Address correspondence to jusheng@suda.edu.cn, mrshen@suda.edu.cn.

Received for review March 28, 2012 and accepted September 16, 2012.

Published online September 17, 2012
10.1021/nn303943t

these perovskite heterostructures. Since the correlation effect plays an important role,[21−23] even in a magnetic analogy of $SrMnO_3/LaMnO_3$ superlattice, spin-polarized conducting states are restricted within a two-atomic thick interface layer.[24−26] Recently, $LaMnO_3/SrMnO_3$, $La_{0.7}Sr_{0.3}MnO_3/SrTiO_3$, $La_{0.7}Sr_{0.3}MnO_3/BaTiO_3$, and $LaMnO_3/SrTiO_3$ heterostructures have been fabricated successfully.[27−39] Despite the appearances of enhanced magnetic ordering temperature, unusual Ti magnetism, and magnetic controllable metal-to-insulator transition in these digital nanostructures, the robust and stable half-metallic state is still not available. First-principles investigations have provided several alternative systems. Ferromagnetic EuO was first proposed to be combined with $LaAlO_3$ to achieve spin-polarized two-dimensional electron gas.[40,41] Recently, highly spin-polarized two-dimensional electron gas was revealed at the interface between $LaAlO_3$ and a nonmagnetic FeS_2,[42] demonstrating its potential application in spintronic devices.

In this paper, we report the realization of half-metallic state *via* the interface electronic reconstruction in a heterostructure of $SrMnO_3/LaAlO_3$ nanosheet superlattice. Since band insulator $LaAlO_3$ acts as charge reservoir with alternately charged atomic layers, and $SrMnO_3$ is an antiferromagnetic band insulator with unoccupied e_g orbitals and possesses charge-neutral atomic layers, an electronic reconstruction based on pure electrostatic charge transfer scenario,[43] rather than strong correlation effect, is expected. In addition, in obvious contrast to $LaMnO_3/SrMnO_3$ systems, both *n*-type and *p*-type interfaces can be well distinguished in $LaAlO_3/SrMnO_3$ superlattices, where LaO/MnO_2 is *n*-type while SrO/AlO_2 is *p*-type. Therefore, various combinations of these two types of interfaces in one superlattice unit are believed to give rise to rich and experimentally accessible properties. In fact, based on extensive first-principles density-functional calculations, we reveal that the electron transfer indeed happens at the $(LaO)^+/(MnO_2)^0$ interface and robust half-metallic ferromagnetism can be realized in the *nn*-type $SrMnO_3/LaAlO_3$ superlattices. Furthermore, for the superlattices with $(SrO)^0/(AlO_2)^-$ heterointerfaces, a magnetic ordering dependent charge transfer and electronic reconstruction are found. In particular, when these systems transit from their ground state to ferromagnetic state by an external magnetic field, an obvious change of the electronic state at the Fermi level is observed. All these results demonstrate unusual magnetic, electric, and magnetotransport properties in these perovskite digital nanostructures.

RESULTS AND DISCUSSION

To study the interface electronic reconstruction explicitly, we consider three kinds of superlattice structures. As demonstrated in Figure 1: superlattices with only *n*-type interfaces (*i.e.*, $(LaO)^+/(MnO_2)^0$ interface),

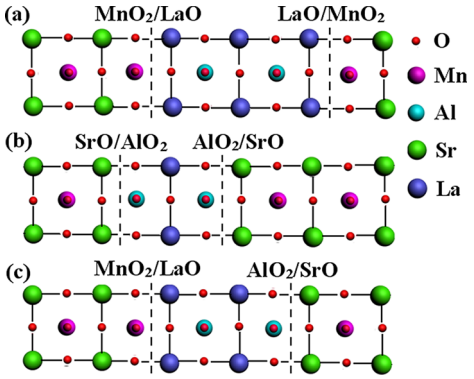

Figure 1. Illustration of three kinds of $LaAlO_3/SrMnO_3$ superlattices: (a) *nn*-type superlattice with 5−3 as an example; (b) *pp*-type superlattice with 5−3 as an example; (c) *np*-type superlattice with 5−3 as an example. Here, *n*-type refers to $(LaO)^+/(MnO_2)^0$ interface and *p*-type is $(SrO)^0/(AlO_2)^-$ interface.

TABLE 1. Total Energies (meV per Mn) in *nn*-Type Superlattices for Various Magnetic Orderings. Bulk $SrMnO_3$ Is Also Shown

	bulk $SrMnO_3$	3−2	4−2	5−2	4−3	5−3	5−4
E (FM)	43.4	0	0	0	0	0	0
E (A-type AFM)	25.3	15.5	14.9	15.0	6.1	6.2	5.0
E (C-type AFM)	12.4	123.5	125.2	125.0	19.0	19.2	1.3
E (G-type AFM)	0	329.1	328.4	328.3	56.7	57.0	156.3

superlattices with only *p*-type interfaces (*i.e.*, $(SrO)^0/(AlO_2)^-$ interface), and superlattices with both *n*-type and *p*-type interfaces. By varying the thickness of both $SrMnO_3$ and $LaAlO_3$ components, quantum confinement effects and the dependence of electric and magnetic properties on the number of MnO_2 layers are well studied. We use *N*−*M* to label our superlattice structure, where *N* is the total number of perovskite units and *M* indicates the number of MnO_2 layers. Similar to $SrTiO_3$, bulk $SrMnO_3$ belongs to $a^0a^0a^0$ in Glazer notation. Therefore, following the previous approaches on $LaAlO_3/SrTiO_3$ heterostructures,[17] we first focus on the symmetry based on bulk $SrMnO_3$ with an optimized in-plane lattice constant of 3.85 Å and try to construct a general picture of charge transfer and interface electronic reconstruction in $LaAlO_3/SrMnO_3$ nanosheet superlattices. Effects of octahedral rotation and titling and their epitaxial strain dependence (for both compressive strain with an in-plane lattice constant of 3.80 Å and tensile strain with an in-plane lattice constant of 3.90 Å) are discussed afterward.

We first demonstrate the electronic band structure of *nn*-type superlattices. Total energies show that among various magnetic orderings, FM ordering is energetically favorable, which is in contrast to G-type AFM magnetic ordering in the bulk $SrMnO_3$ (see Table 1). Clearly, as demonstrated in Figure 2, a half-metallic electronic structure is revealed in all the cases. The itinerating states at the Fermi level arise mainly from the fully spin-polarized Mn ions. In addition, the band gap in the

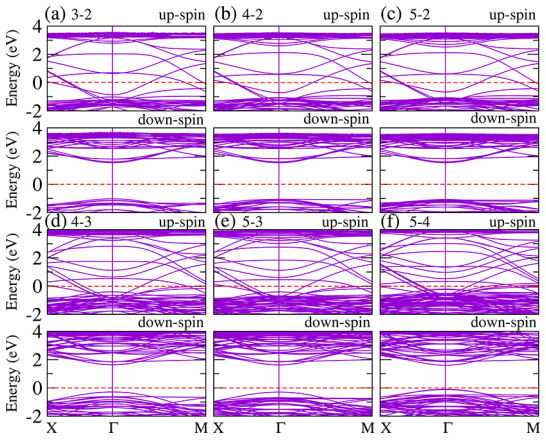

Figure 2. Electronic band structure of *nn*-type superlattices. (a) 3−2, (b) 4−2, (c) 5−2, (d) 4−3, (e) 5−3, and (f) 5−4. The half-metallic state is found in all the cases. Fermi level is at energy zero (dashed line).

spin-down channel is around 2.5 eV, much larger than conventional electron-doped bulk $SrMnO_3$, for example, 1 eV in $La_{0.67}Sr_{0.33}MnO_3$.[44−46] This is due to quantum confinement effects, making the localized spin-down t_{2g} states much narrower in energy scale and exchange-splitting stronger. With increasing $SrMnO_3$ layers, the top of the valence band moves close to the Fermi energy and the gap in the spin-down channel decreases to 2 eV. It should be pointed out that the bottom of the conduction band in the spin-down channel is almost fixed at the Γ point. When the number of MnO_2 layers increases further, as that in the *nn*-type 5−4 superlattice, the top of valence band of spin down channel is very close to the Fermi level, but the spin down channel remains semiconducting. Therefore, an overall half-metallic ferromagnetism can be safely realized in all the *nn*-type superlattices we considered. Also, judging from the energy differences between the FM ground state and other AFM ordering (see Table 1), one can expect the large magnetic exchange coupling strength and consequently high Curie temperature in these *nn*-type superlattices. Here, for the two-dimensional nature of the superlattice structure, magnetic exchange interactions exhibit obvious anisotropic behaviors, with interplane coupling being much smaller than intraplane coupling. This point can be deduced from the smaller energy difference between A-type AFM and FM orderings than that between C-type AFM and FM orderings. On the other hand, we find that the energy difference between G-type AFM and FM orderings in $La_{3/4}Sr_{1/4}MnO_3$ is 426.7 meV/Mn, which is close to our studied *nn*-type N-2 superlattices and exhibits the Curie temperature of 333 K.[46] Therefore, the Curie temperature of a similar order in *nn*-type superlattices should be smaller than the bulk manganites. In addition, it should be pointed out that the half-metallic electronic state in the *nn*-type superlattices is very robust upon the choice of parameter Hubbard *U*, where our additional calculations based on a smaller *U* of 2 eV also give rise to the half-metallicity.

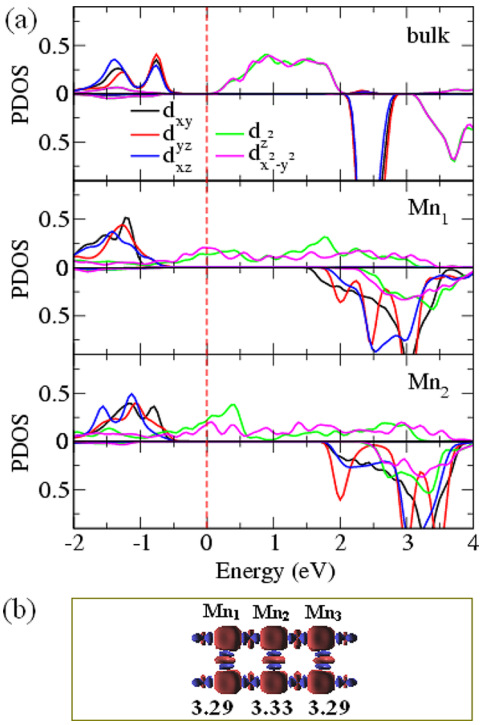

Figure 3. (a) Orbital resolved local density of states at Mn sites in bulk $SrMnO_3$ and a typical *nn*-type 5−3 superlattice. The Fermi level is at energy zero with dashed line indicated. (b) Corresponding spin-density and local magnetic moment (μ_B/Mn) of three MnO_2 layers. For the symmetric superlattice structure, Mn_1 and Mn_3 are similar with each other.

To understand the driving mechanism of half-metallic electronic structure in *nn*-type $LaAlO_3/SrMnO_3$ superlattices further, we show the orbital resolved local density of states in a typical *nn*-type superlattice of 5−3 (see Figure 3a). Formerly unoccupied e_g states in bulk $SrMnO_3$ now get partially occupied, and both $d_{x^2-y^2}$ and d_{z^2} states are observed at the Fermi level. The detailed e_g orbital occupation number is found to be almost a constant within the $SrMnO_3$ component, indicating the uniform distribution of transferred electrons from adjacent $(LaO)^+$ layers. For the occupation of the e_g states, the charge transfer at the $(LaO)^+/(MnO_2)^0$ interface indeed happens in the *nn*-type superlattices. In addition, the magnetic moment at Mn sites in 3−2, 4−2, and 5−2 cases, is around 3.5 μ_B. In 4−3 and 5−3, it is around 3.3 μ_B. For 5−4, the local magnetic moment is around 3.2 μ_B. The gradual decrease of local magnetic moment with the increase of MnO_2 layers also verifies the fact that the total transferred charges across the $(LaO)^+/(MnO_2)^0$ interfaces is fixed. The spin-densities (of all the valence electrons) show the coexistence of fully spin-polarized t_{2g} states and e_g states at Mn sites (see Figure 3b). It is noted that Zener double-exchange lies at the heart of the description of half-metallic electronic ferromagnetism in the doped manganites.[47,48] Within this picture, itinerating e_g electrons coexist with the localized t_{2g} spins, which agrees with our findings in these *nn*-type

TABLE 2. Total Energies (meV per Mn) in *pp*-Type Superlattices for Various Magnetic Orderings

	bulk $SrMnO_3$	3–1	4–1	5–1	4–2	5–2	5–3
E (FM)	43.4	38.4	36.0	35.3	40.7	38.9	40.0
E (A-type AFM)	25.3	0	0	0	33.9	33.8	31.7
E (C-type AFM)	12.4	0	0	0	2.0	1.7	2.3
E (G-type AFM)	0	0	0	0	0	0	0

superlattices. In our studied two-dimensional nanosheet superlattices, we find that one net electron is transferred into the $SrMnO_3$ component, and the half-metallicity can be found in a range, where e_g electron per Mn is from 0.25 to 0.5. These findings demonstrate distinct aspects of these two-dimensional systems from the conventional bulk systems of electron-doped $SrMnO_3$, where half-metallic ferromagnetism can be only observed at the so-called optimized doping level such as $La_{0.7}Sr_{0.3}MnO_3$ and $La_{2/3}Sr_{1/3}MnO_3$.[44−46] In addition, from the phase diagram of $La_{1-x}Sr_xMnO_3$, FM phase develops from $x = 0.16$ to $x = 0.48$, where e_g orbital occupation is from 0.52 to 0.84.[46] And when e_g orbital occupation is lower than 0.52, AFM ordering is preserved.[46]

Next, we move to the *pp*-type $LaAlO_3/SrMnO_3$ superlattices. From the total energies as listed in Table 2, it is revealed that G-type antiferromagnetic (AFM) ordering is the ground state, where Mn ions coupled antiferromagnetically both in the *ab*-plane and along the *c* axis. In these *pp*-type superlattices, the formerly unoccupied e_g states are still empty. And the local magnetic moment at the Mn sites is around 2.9 μ_B, much smaller than the 3.5 μ_B in the *nn*-type superlattices (see Figure 4). The detailed band structure is shown in Figure 5. Unlike bulk $SrMnO_3$ or $LaAlO_3$, *pp*-type superlattices are metallic, and the Fermi level is just across the top of valence bands and the density of states at the Fermi level are mainly from oxygen, showing the obvious *p*-type characteristics as that in *pp*-type $LaAlO_3/SrTiO_3$ superlattices.[17] The polar electric field in the $LaAlO_3$ will drive holes out of the $LaAlO_3$ component and into $SrMnO_3$ at the *p*-type interface, but once in the $SrMnO_3$, the holes do not have any reason to be bound to the interface. Judging from the density of states as shown in Figure 6 for a typical 5−3 case, the holes reside almost uniformly at the oxygen atoms in the superlattice and t_{2g} orbitals at the Mn sites are still fully occupied. Because of the absence of the e_g states at the Mn sites, the development of bulk-like G-type AFM ordering in the *pp*-type superlattices is obvious.

Here, we would like to emphasize the following aspects in manganite bulk systems. t_{2g} orbitals interact by superexchange and their contribution is negative (AFM), whereas the $d_{z^2}-d_{z^2}$ interaction is positive (FM). Also positive are the $d_{x^2-y^2}-d_{z^2}$ and the much weaker $d_{x^2-y^2}-d_{x^2-y^2}$. In addition, the nature of magnetic ordering in manganites, including $LaMnO_3$, $SrMnO_3$,

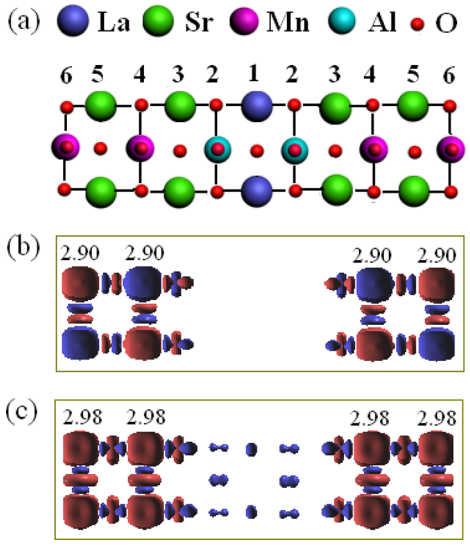

Figure 4. Change of spin-density in *pp*-type 5−3 superlattice. (a) Crystal structure with six inequivalent planes (1−6). (b) Corresponding spin-density and local magnetic moment (μ_B/Mn) in the ground state (G-type AFM). (c) Corresponding spin-density and local magnetic moment (μ_B/Mn) in FM state.

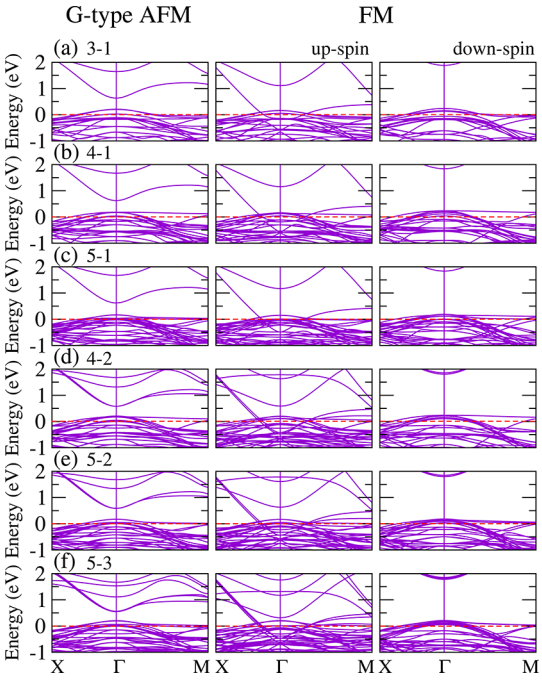

Figure 5. Electronic band structure of *pp*-type superlattices within both the ground state (G-type AFM) and FM state. For the G-type AFM ordering, up-spin and down-spin channels are degenerated. (a) 3−1, (b) 4−1, (c) 5−1, (d) 4−2, (e) 5−2, and (f) 5−3. Fermi level is at energy zero (dashed line).

and a wide range of doping conditions, is the balance between competing AFM superexchange, FM double-exchange, and other mechanisms. Within the double-exchange, FM interaction is mediated by the hopping of e_g electrons. In the bulk $SrMnO_3$, Mn^{4+} ions are AFM coupled owing to the absence of e_g electrons. Whereas e_g orbitals are completely filled as that in

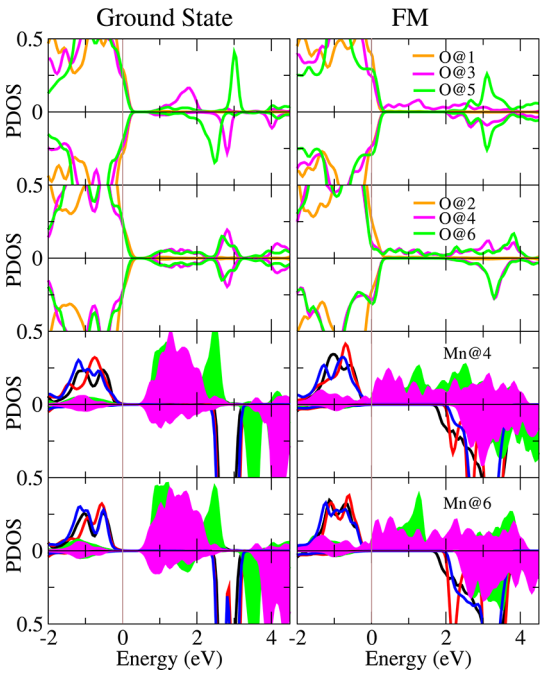

Figure 6. Partial density of states at *pp*-type 5−3 superlattices. Both oxygen and manganese ions at different planes (from plane 1 to plane 6 as shown in Figure 4) are plotted. Left panels for the ground state and right panels for FM state. The shaded area is for Mn e_g orbitals (with green for d_{z^2} and magenta for $d_{x^2-y^2}$). Fermi level is at energy zero (dashed line).

MnO, AFM coupling also develops. FM ordering therefore develops only when e_g orbitals are partially filled.[48] However, in the *pp*-type $LaAlO_3/SrMnO_3$ superlattices, charge transfer happens at the $(AlO_2)^-/(SrO)^0$ interface and the transferred hole penetrates into the $SrMnO_3$ component. The hole shows the characteristics of oxygen *p* orbitals and resides mainly at interlayer oxygen sites, leading to the modification of the magnetic interaction in the interlayer $Mn^{4+}-O^{-2+\delta}-Mn^{4+}$ path. In addition, in the quasi-two-dimensional superlattice structure, the magnetic ordering is also susceptible with quantum confinement effects of t_{2g} orbitals. Here, d_{xy} orbitals are extended in the *ab* plane and AFM coupling is preserved between intralayer Mn ions. But because of the confined d_{xz} and d_{yz} orbitals, FM coupling can be favored between the interlayer Mn ions, and therefore, alternative C-type AFM ordering can be stabilized by the combined depleted charge at the oxygen sites and the geometry confinement in *pp*-type superlattices. Such a kind of C-type AFM ordering is found either for larger *U* of 4 eV or for the situation with compressive epitaxial strain.

It should be pointed out that in our approach, we focus on the magnetic-ordering related interface electronic reconstruction, whereas we use symmetric superlattices to deal with *n*-type and *p*-type interfaces, indicating the thick $LaAlO_3$ limit.[17] As shown in Figure 7, we demonstrate the basic picture at these *n*-type and *p*-type heterointerfaces. At the *n*-type interface,

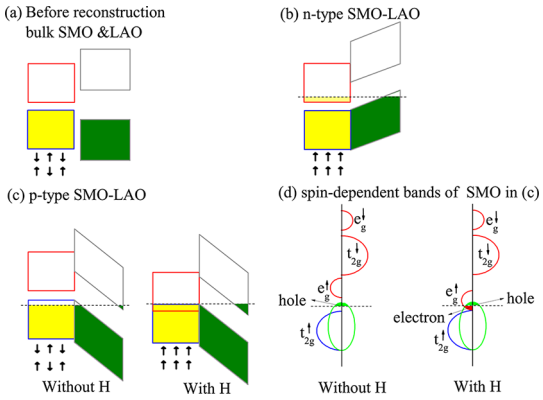

Figure 7. Illustration of band diagram at $LaAlO_3/SrMnO_3$ interface: (a) Bulk $SrMnO_3$ with G-type AFM ordering and $LaAlO_3$; (b) *n*-type interface with electron transferred into $SrMnO_3$; (c) *p*-type interface with hole transferred into $SrMnO_3$. In this case, both the ground state with G-type AFM ordering and FM state under external magnetic field are plotted. (d) Detailed spin-resolved band structure of $SrMnO_3$ at the *p*-type interface.

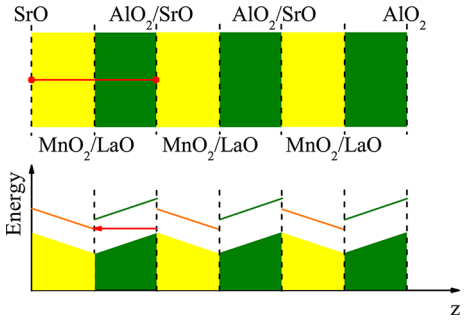

Figure 8. Illustration of energy diagram and corresponding electrostatics potential in *np*-type superlattices: (yellow) $SrMnO_3$; (green) $LaAlO_3$.

electrons are transferred across the interface, and the $SrMnO_3$ becomes half-metal *via* the double-exchange mechanism. While at the *p*-type interface, holes leak into oxygen sites in $SrMnO_3$, and Mn e_g orbitals are still empty. When a magnetic field is applied to induce FM ordering, the *p*-type interface shows the characteristics of coexistence of electron-doping and hole-doping, suggesting unusual magnetotransport properties therein.

So far, we have understood the electronic reconstruction at both *n*-type and *p*-type heterointerfaces within the symmetric *nn*-type and *pp*-type superlattices. Now we focus on the *np*-type superlattices, where, from the point of view of stoichiometry, the system looks charge neutral and might be bulk-like as the lattices respective components. However, as shown in Figure 8, the zigzag potential profile inherent to this asymmetric structure will lead to obvious thickness-dependent charge transfers in these *np*-type superlattices. As shown in Tables 3 and 4, complex magnetic orderings develop in the *np*-type superlattices, depending strongly on the number of MnO_2 layers as well as the thickness of the $LaAlO_3$ component. Compared with bulk G-type AFM-ordered $SrMnO_3$ (2.8 μ_B/Mn), the local

TABLE 3. Ground-State Spin-Configuration and Corresponding Local Magnetic Moment (μ_B/Mn) in *np*-Type Superlattices. For Each Case, The Left-Hand Side Is *p*-Type Interface and the Right-Hand Side is *n*-Type Interface

2—1	3—1	4—1	5—1	3—2	4—2	5—2	4—3	5—3	5—4
↑	↑	↑	↑	↑↓	↑↓	↑↑	↑↓↑	↑↓↑	↑↓↑↓
↓	↑	↑	↑	↓↑	↓↑	↓↑	↓↑↓	↓↑↓	↓↑↓↑
2.9	3.0	3.0	3.0	2.9/2.9	2.9/2.9	2.9/3.0	2.9/2.9/2.9	2.9/2.9/2.9	2.9/2.9/2.9/2.9

magnetic moment at Mn sites is a little enhanced and reaches 2.9 μ_B for 2—1 and 3.0 μ_B for 3—1, 4—1, and 5—1 cases, and such an enhancement is also observed in 3—2, 4—2, and 5—2 cases as well as in 4—3, 5—3, and 5—4 cases. These enhanced local magnetic moments indicate the occupation of e_g orbitals at Mn sites. For the single MnO_2 layer (including 2—1, 3—1, 4—1, and 5—1), AFM ordering is found for the thinnest $LaAlO_3$ layer (*i.e.* *np*-type 2—1). With increasing $LaAlO_3$ layer, FM ordering is preferred when the number of $LaAlO_3$ layers is larger than two, where the polar field arising from the $LaAlO_3$ component is large enough to induce electron transfer at the heterointerfaces. As also demonstrated in Figure 9, these systems are normal ferromagnets, where finite density of states is found at the Fermi level of the spin-down channel. For the 3—2 and 4—2 superlattices, bulk-like G-type AFM ordering is found. However, when the $LaAlO_3$ layer reaches three as in 5—2, FM intralayer coupling is found near the *n*-type interface. For three-layered Mn systems (including 4—3 and 5—3) and four-layered 5—4, G-type AFM ordering is identified. In Figure 10, we plot the position-dependent DOS for 5—3. Therefore, one can conclude that FM ordering could develop near the side of *n*-type interface when $LaAlO_3$ component is thick enough to induce charge transfer at the interfaces. When moving away from the *n*-type interface to the *p*-type interface, bulk-like G-type AFM ordering is preferred. All these results suggest that electron transfer gets started at the $(LaO)^+/(MnO_2)^0$ interface, weakens gradually when penetrating into $SrMnO_3$ component, and finally stops at $(AlO_2)^-/(SrO)^0$ interface. In the mean time, holes of similar quantity are transferred at the $(AlO_2)^-/(SrO)^0$ interface, making the systems charge neutral. These transferred electrons and holes will renormalize the magnetic interaction strengths between neighboring Mn sites, and consequently the appearance of complex and graded ground-state magnetic ordering in *np*-type superlattices.

With regarding to above findings, here we would like to remark that doped manganites often show colossal magnetoresistive effects. The magnitude relies on the doping level and the contrast in the electronic structure between the ground state and FM state, for example, metal versus insulator or half-metal versus normal ferromagnet. In fact, in Figure 5 and Figure 11, we also show the electronic band structure of *pp*-type and *np*-type superlattice within FM ordering. An obvious change of band structure at the Fermi level is observed in *pp*-type superlattices, where compared with G-type AFM state, fully spin-polarized Mn e_g bands with higher mobility (compared with the flat bands from oxygen near Fermi level) get across the Fermi level in the FM state. For *np*-type superlattices, such e_g bands shift from spin-down channel to spin-up channel, leading to an obvious contrast in spin-polarization between the ground state and FM state. In addition, in *np*-type superlattices, with increasing $LaAlO_3$ layers, a tendency of transition from a complex AFM state to FM state is expected, and the energy difference between them gets smaller and smaller. For example, the energy difference is 25.6 meV/Mn in the *np*-type 3—2 and is decreased to 9.8 meV/Mn in the 4—2, and finally the system transits to complex magnetic ordering ground state with energy difference of 7.7 meV/Mn in the 5—2. These results suggest that possible colossal magnetoresistive effects *via* the phase competition can be observed when an external magnetic field is applied in these *np*-type $LaAlO_3/SrMnO_3$ superlattices.

TABLE 4. Total Energies (meV per Mn) of *np*-Type Superlattices with Various Kinds of Spin-Configurations. For Each Case, The Left-Hand Side Is *p*-Type Interface and the Right-Hand Side Is *n*-Type Interface

		spin			↑			↑	
		configuration			↑			↓	
$N-1$	2—1				10.9			0	
	3—1				0			3.8	
	4—1				0			12.8	
	5—1				0			20.4	
		spin	↑↓	↑↑	↑↓	↑↑	↑↑	↑↑	
		configuration	↑↓	↓↓	↓↑	↑↑	↓↑	↑↓	
$N-2$	3—2		15.9	5.0	0	25.6	12.5	8.5	
	4—2		3.3	3.8	0	9.8	6.9	5.7	
	5—2		2.0	12.9	9.1	7.7	0	8.9	
		spin	↑↓↑	↑↑↑	↑↓↑	↑↑↑	↑↑↑	↓↑↑	↑↓↑	↑↓↓	↑↓↓
		configuration	↑↓↑	↓↓↓	↓↑↓	↑↑↑	↓↑↑	↓↓↑	↓↑↓	↓↑↓	↓↑↑
$N-3$	4—3		17.5	6.4	0	28.0	19.1	16.2	12.5	5.5	2.9
	5—3		5.8	5.1	0	13.7	8.3	5.8	2.8	1.6	2.7
		spin	↑↓↑↓	↑↑↑↑	↑↓↑↓	↑↑↑↑	↓↑↓↓	↑↓↓↑	↑↓↑↑		
		configuration	↑↓↑↓	↓↓↓↓	↓↑↓↑	↑↑↑↑	↑↓↓↓	↓↑↓↑	↓↑↓↑		
$N-4$	5—4		18.3	8.1	0	28.5	14.3	9.0	4.0		

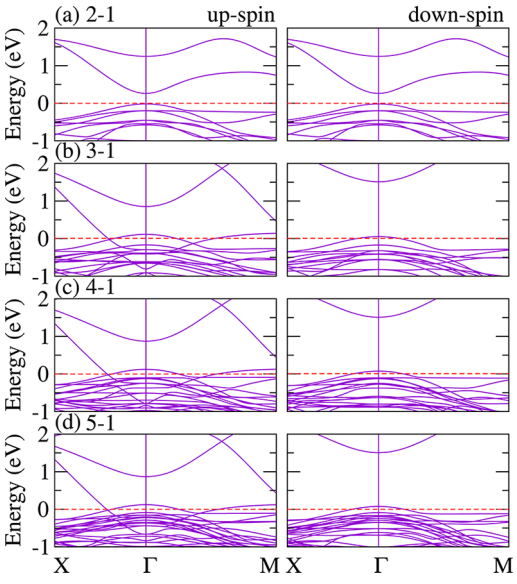

Figure 9. Band structure of *np*-type 2−1 (a), 3−1 (b), 4−1 (c), and 5−1 (d) superlattices within their ground state. Fermi level is at energy zero (dashed line).

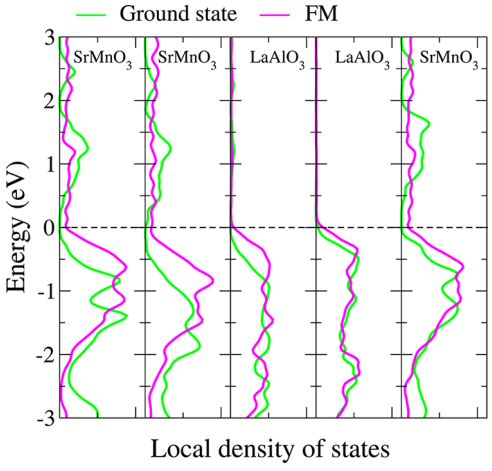

Figure 10. Local density of states (majority spin channel) in *np*-type 5−3 superlattice. Fermi level is at energy zero (dashed line).

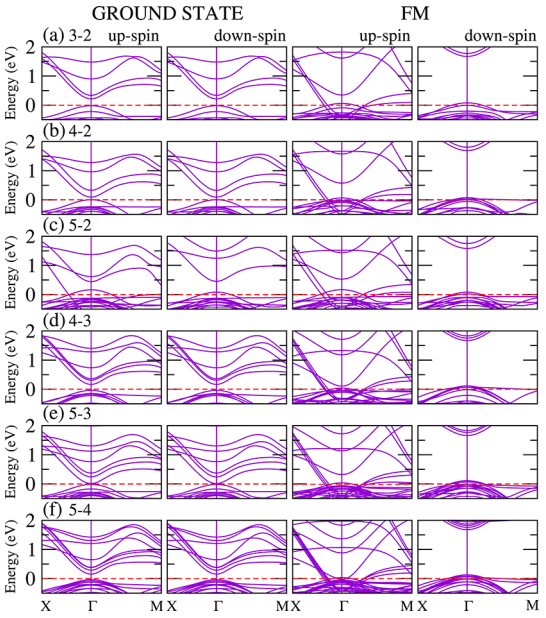

Figure 11. Electronic band structure of *np*-type superlattices within both the ground state and FM state: (a) 3−2, (b) 4−2, (c) 5−2, (d) 4−3, (e) 5−3, and (f) 5−4. Fermi level is at energy zero (dashed line).

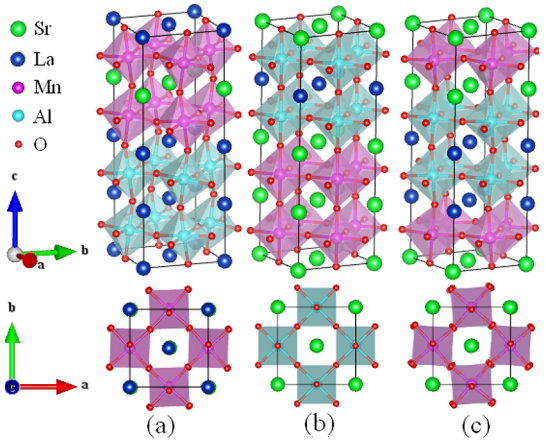

Figure 12. Illustration of crystal structure of $LaAlO_3/SrMnO_3$ superlattices with the presence of oxygen octahedra rotation and tilting: (a) *nn*-type 4−2, (b) *pp*-type 4−2, and (c) *np*-type 4−2.

Finally, we consider the effects of oxygen octahedra rotation and tilting and their epitaxial strain dependence. These effects are believed to play an important role in transition metal oxides, in particular for the Jahn−Teller active systems.[49,50] For the coherent rotation and tilting, we use 4−*M* as model system (see Figure 12 and the Supporting Information for the details). The ground-state magnetic ordering and energetics are summarized in Table 5 and 6, respectively. The results within $SrMnO_3$ bulk symmetry are also demonstrated. For the *nn*-type superlattice 4−2, half-metallicity is preserved when epitaxial strain is imposed. The inclusion of oxygen octahedra rotation and tilting does not change the observation of robust half-metallic electronic state therein. However, in *nn*-type 4−3, C-type AFM ordering and A-type AFM ordering are revealed for compressive and tensile strains, respectively. The origin can be judged easily from Figure 13, where two e_g orbitals are plotted. A-type AFM ordering is favored by the occupation of $d_{x^2-y^2}$, while C-type AFM ordering is due to preference of d_{z^2} with a gap opened near the Fermi level. When the oxygen octahedra rotation and tilting are considered, either C-type AFM ordering under compressive strain or A-type AFM ordering under tensile strain is found to transit to FM ordering, with half-metallicity recovered. Therefore, we can conclude that when the e_g electron at Mn ions is nonzero, the Jahn−Teller distortion accompanied with oxygen octahedra rotation and tilting is energetically favorable. In addition, for the

TABLE 5. Ground-state Spin-Configuration of 4—*M* Superlattices with Different Strain Conditions and Crystal Symmetries[a]

	3.80 Å		3.85 Å		3.90 Å	
	w/o	with	w/o	with	w/o	with
nn-type 4—2	↑↑	↑↑	↑↑	↑↑	↑↑	↑↑
	↑↑	↑↑	↑↑	↑↑	↑↑	↑↑
nn-type 4—3	↑↑↑	↑↑↑	↑↑↑	↑↑↑	↑↓↑	↑↑↑
	↓↓↓	↑↑↑	↑↑↑	↑↑↑	↑↓↑	↑↑↑
pp-type 4—1	↑	↑	↑	↑	↑	↑
	↓	↓	↓	↓	↓	↓
pp-type 4—2	↑↑	↑↑	↑↓	↑↓	↑↓	↑↓
	↓↓	↓↓	↓↑	↓↑	↓↑	↓↑
np-type 4—1	↑	↑	↑	↑	↑	↑
	↑	↑	↑	↑	↑	↑
np-type 4—2	↑↓	↑↓	↑↓	↑↓	↑↓	↑↓
	↓↑	↑↓	↓↑	↑↓	↑↓	↑↓
np-type 4—3	↑↓↑	↑↓↑	↑↓↑	↑↓↑	↑↓↑	↑↓↑
	↓↑↓	↓↑↑	↓↑↓	↓↑↑	↓↑↑	↓↑↑

[a] Here, "w/o" and "with" mean without and with consideration of oxygen octahedra rotation and tilting, respectively. For each case, the left-hand side is *p*-type interface and the right-hand side is *n*-type interface.

TABLE 6. Ground-State Energetics (meV per Mn) in 4—*M* Superlattices for Different Strain Conditions and Crystal Symmetries[a]

	3.80 Å		3.85 Å		3.90 Å	
	w/o	with	w/o	with	w/o	with
nn-type 4—2	134.4	93.5	53.7	16.7	54.3	0
nn-type 4—3	48.8	41.3	30.1	13.6	20.4	0
pp-type 4—1	22.7	21.5	0	3.4	112.5	118.5
pp-type 4—2	18.4	16.8	0	0.6	54.7	52.1
np-type 4—1	64.0	6.5	45.7	0	178.5	121.4
np-type 4—2	32.7	17.0	18.5	0	65.8	46.5
np-type 4—3	33.2	12.5	15.4	0	48.2	30.5

[a] Here, "w/o" and "with" mean without and with consideration of oxygen octahedra rotation and tilting, respectively.

shift of Mn—O—Mn angle away from 180°, FM coupling is more preferred between Mn ions. For *pp*-type superlattices, magnetic ordering of single MnO_2 layered *pp*-type 4—1 does not change. For 4—2, G-type AFM ordering changes to C-type one under compressive strain. As shown in Figures 14, 15, and 16, for these *p*-type interfaces, the distribution of holes at oxygen sites changes significantly with strain. With increasing in-plane lattice constant, an obvious shift of Fermi level to higher energies is observed, making the holes residing at oxygen sites fewer and FM coupling weakened. The inclusion of oxygen octahedra rotation and tilting does not change the ground-state magnetic ordering. For *np*-type superlattices, the charge transfer arising from the polar field is susceptible to epitaxial strain. In *np*-type 4—1, FM ordering does not change upon epitaxial strain. For the case of *np*-type 4—2 (see Figure 17),

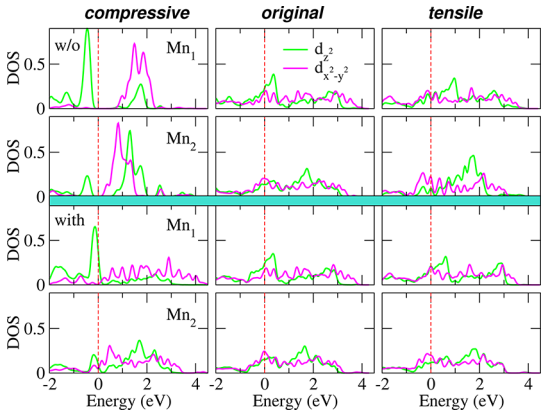

Figure 13. DOS of Mn e_g orbitals in *nn*-type 4—3 superlattice. Up panels and down panels are for the situations without (w/o) and with considering oxygen octahedra rotation and tilting, respectively. The dashed line is for Fermi level. Here, Mn_2 is near the *n*-type interface and Mn_1 is in the middle.

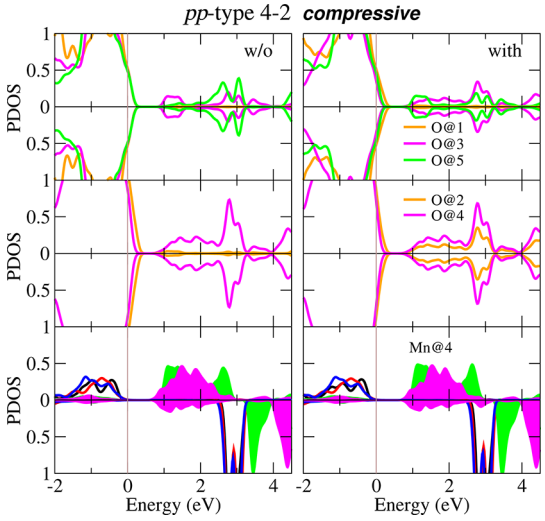

Figure 14. Partial density of states in *pp*-type 4—2 superlattices under compressive strain. Both oxygen and manganese ions at different planes are plotted. Left panels and right panels are for the situations without (w/o) and with considering oxygen octahedra rotation and tilting, respectively. The shaded area is for e_g orbitals (with green for d_{z^2} and magenta for $d_{x^2-y^2}$) at Mn ions. The dashed line is for Fermi level. Layers 1—5 are similar with those in Figure 4(a) for *pp*-type 5—3 but with layer 6 omitted in 4—2.

G-type AFM ordering transits to A-type AFM ordering for tensile strain. This is due to the increase of polar field for the shortening of the *z* axis. On the other hand, oxygen octahedra rotation and tilting are found to lead to similar results, where A-AFM ordering is also found. For the case of *np*-type 4—3 (see Figure 18), similar observations are observed and FM intralayer coupling develops near the *n*-type interface. All the above results show the strengthened FM coupling between neighboring Mn ions when oxygen rotation and tilting are present. With the above findings, we have provided a comprehensive picture of electronic and magnetic reconstructions in $LaAlO_3/SrMnO_3$ superlattices. Compared

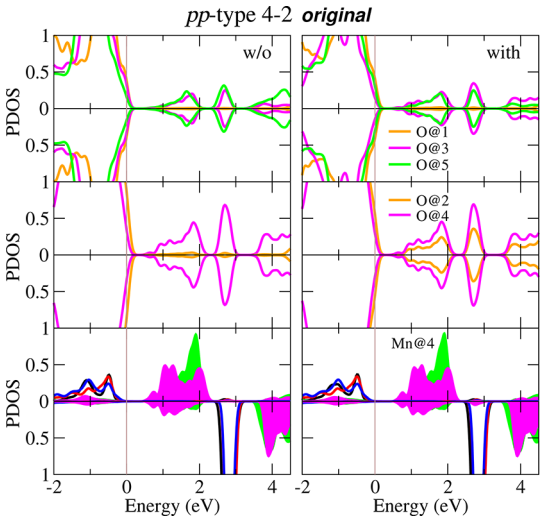

Figure 15. Partial density of states in *pp*-type 4−2 superlattices without strain. Both oxygen and manganese ions at different planes are plotted. Left panels and right panels are for the situations without (w/o) and with considering oxygen octahedra rotation and tilting, respectively. The shaded area is for e_g orbitals (with green for d_{z^2} and magenta for $d_{x^2-y^2}$) at Mn ions. The dashed line is for Fermi level.

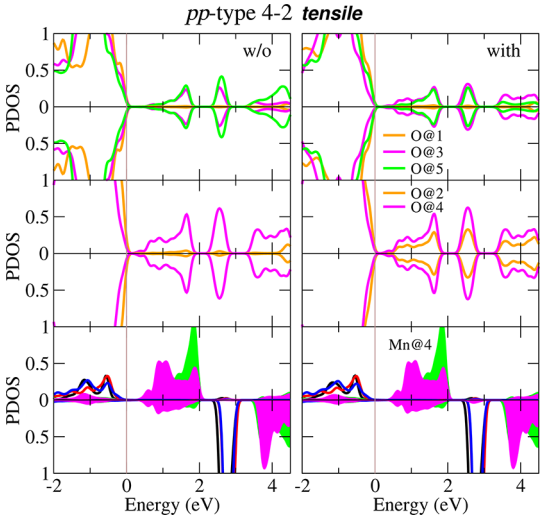

Figure 16. Partial density of states in *pp*-type 4−2 superlattices under tensile strain. Both oxygen and manganese ions at different planes are plotted. Left panels and right panels are for the situations without (w/o) and with considering oxygen octahedra rotation and tilting, respectively. The shaded area is for e_g orbitals (with green for d_{z^2} and magenta for $d_{x^2-y^2}$) at Mn ions. The dashed line is for the Fermi level.

with the $LaMnO_3/SrMnO_3$ heterointerface and bulk $La_xSr_{1-x}MnO_3$, $LaAlO_3/SrMnO_3$ superlattices show a different phase diagram. In particular, half-metallic ferromagnetism in *nn*-type superlattices is found in a wide range of e_g electron doping. For *pp*-type $LaAlO_3/SrMnO_3$ superlattices, the hole-doping effect in $SrMnO_3$ is studied for the first time, where the depleted oxygen tends to give rise to FM coupling, providing an alternative mechanism for FM ordering in manganites systems.

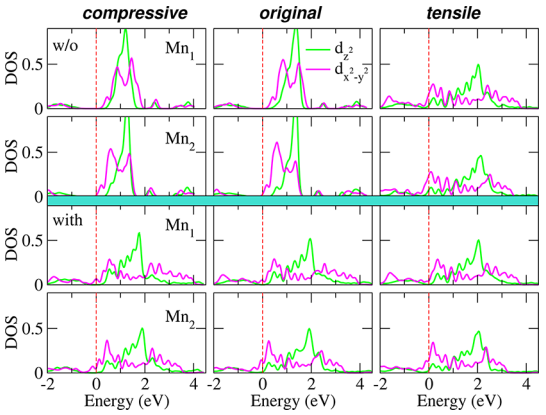

Figure 17. DOS of Mn e_g orbitals in *np*-type 4−2 superlattice. Top panels and bottom panels are for the situations without (w/o) and with considering oxygen octahedra rotation and tilting, respectively. The dashed line is for Fermi level. Here, Mn_2 is near the *n*-type interface and Mn_1 is near the *p*-type one.

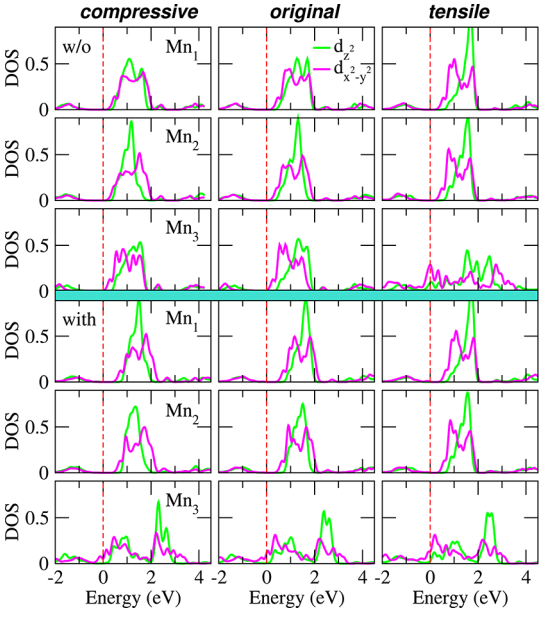

Figure 18. DOS of Mn e_g orbitals in *np*-type 4−3 superlattice. Top panels and bottom panels are for the situations without (w/o) and with considering oxygen octahedra rotation and tilting, respectively. The dashed line is for Fermi level. Here, Mn_3 is near the *n*-type interface, Mn_1 is near the *p*-type one, and Mn_2 is in the middle.

Moreover, the charge-neutral *np*-type superlattices are found to exhibit complex magnetic ordering and consequently possible colossal magnetoresistive effects *via* phase competition.

CONCLUSIONS

We have realized a robust half-metallic electronic state and significant magnetoresistive effect *via* the interface electronic reconstruction in $LaAlO_3/SrMnO_3$ nanosheet superlattices. The effects of epitaxial strain, oxygen octahedra rotation and tilting, and Coulomb correlation are studied in details. Using first-principle density-functional calculations, we have shown that

half-metallic ferromagnetism is stabilized in *nn*-type superlattices, where the averaged e_g electron per Mn is from 0.5 in $N-2$ systems to 0.25 in $N-4$ systems. For *pp*-type and *np*-type superlattices, although AFM coupling is favored between Mn ions, an obvious change of electronic structure at Fermi level can be found when the systems are switched to FM ordering *via* external magnetic field. In particular, in *np*-type superlattices, with increasing $LaAlO_3$, a tendency of transition from complex AFM ordering to FM one is expected, and the energy difference between ground state and FM state can be very small, making the colossal magnetoresistive accessible experimentally. These unusual magnetic and electric properties demonstrate novel emergent phenomena arising from a magnetic ordering dependent interface electronic reconstruction in transition metal oxides and their potential application in spintronic devices.

THEORETICAL METHODS

Our *ab initio* calculations are performed using the accurate full-potential projector augmented wave (PAW) method,[51] as implemented in the Vienna *ab initio* Simulation Package (VASP).[52] They are based on density-functional theory (DFT) with the generalized gradient approximation (GGA) in the form proposed by Perdew, Burke, and Ernzerhof (PBE).[53] On-site Coulomb correlation is included in GGA+*U* approach with the effective Hubbard $U = 3$ eV for M_n 3d orbitals.[54] For the undoped $SrMnO_3$, *U* around 2−3 eV was used.[55,56] However, for $LaMnO_3$, where the number of e_g electron at the Mn site is 1, a larger *U* of 8 eV is needed to stabilize the orbital ordering and A-type AFM ordering.[57] For the partially doped $SrMnO_3$ or $CaMnO_3$, moderate *U* around 3−6 eV were adopted.[58] In our studied $LaAlO_3/SrMnO_3$ superlattices, the maximum e_g orbital occupation is 0.5, as those of *nn*-type $N-2$. In addition, as shown in the Supporting Information for *U*-dependence of ground-state magnetic ordering at various volumes, the Coulomb correlation is found to strengthen FM coupling in $SrMnO_3$ and FM ordering may be overestimated when *U* is larger than 4 eV. Therefore, due to the involvement of the e_g orbital degree of freedom in $LaAlO_3/SrMnO_3$ superlattices, we focus on the calculations based on $U = 3$ eV, where the on-site Coulomb correlation is included and the optimized lattice constant is 3.85 Å, in good agreement with previous first-principles results.[56] Nevertheless, the effects of Coulomb correlation is discussed throughout the context for all kinds of superlattices with either smaller or larger Hubbard *U*. A large plane-wave cutoff of 600 eV is used throughout and the convergence criteria for energy is 10^{-6} eV. PAW potentials are used to describe the electron−ion interaction, with 10 valence electrons for Sr ($4s^2 4p^6 5s^2$), 13 for Mn ($3p^6 3d^5 4s^2$), 9 for La ($5p^6 5d^1 6s^2$), 3 for Al ($3s^2 3p^1$), and 6 for O ($2s^2 2p^4$). A $12 \times 12 \times 4N$ (*N* is the total number of ABO_3 perovskite unit) Monkhorst-Pack *k*-point mesh centered at the Γ point is used.[59] In the calculations, ions are relaxed toward equilibrium positions until the Hellman-Feynman forces are less than 1 meV/Å. In addition, the in-plane lattice constant is fixed and the lattice constant along the *z* axis is optimized. For the electronic density of states, a much larger *k*-mesh of $24 \times 24 \times 8N$ is adopted in Brillouin zone integrations. We use an in-plane $\sqrt{2}a \times \sqrt{2}a$ geometry (with *a* for the in-plane lattice constant of perovskite ABO_3) for the search of the ground-state magnetic ordering. Besides G-type AFM, C-type AFM, A-type AFM, and FM orderings, we also consider and check all the possible linear combination of these orderings.

Conflict of Interest: The authors declare no competing financial interest.

Acknowledgment. We appreciate Prof. Guang-Yu Guo (National Taiwan University) for his useful suggestions and discussions. This work was supported by the National Natural Science Foundation of China under Grants No. 10974140 and No. 11104193. M. R. Shen appreciates the support from the Project Funded by the Priority Academic Program Development of Jiangsu Higher Education Institutions (PAPD).

Supporting Information Available: Detailed volume dependence of bulk $SrMnO_3$ with different magnetic orderings and Hubbard *U*, and strain dependence of crystal structures with the inclusion of oxygen octahedra rotation and tilting. This material is available free of charge *via* the Internet at http://pubs.acs.org.

REFERENCES AND NOTES

1. Wolf, S. A.; Awschalom, D. D.; Buhrman, R. A.; Daughton, J. M.; von Molnr, S.; Roukes, M. L.; Chtchelkanova, A. Y.; Treger, D. M. Spintronics: A Spin-Based Electronics Vision for the Future. *Science* **2001**, *294*, 1488–1495.
2. Zutic, I.; Fabian, J.; Das Sarma, S. Spintronics: Fundamentals and Applications. *Rev. Mod. Phys.* **2004**, *76*, 323–410.
3. Fert, A. Nobel Lecture: Origin, Development, and Future of Spintronics. *Rev. Mod. Phys.* **2008**, *80*, 1517–1530.
4. Grünberg, P. A. Nobel Lecture: From Spin Waves to Giant Magnetoresistance and Beyond. *Rev. Mod. Phys.* **2008**, *80*, 1531–1540.
5. Katsnelson, M. I.; Irkhin, V. Yu.; Chioncel, L.; Lichtenstein, A. I.; de Groot, R. A. Half-Metallic Ferromagnets: From Band Structure to Many-Body Effects. *Rev. Mod. Phys.* **2008**, *80*, 315–378.
6. Son, Y. -W.; Cohen, M. L.; Louie, S. G. Half-Metallic Graphene Nanoribbons. *Nature* **2006**, *44*, 347–349.
7. Shen, L.; Yang, S. -S.; Ng, M. F.; Ligatchev, V.; Zhou, L. P.; Feng, Y. P. Charge-Transfer-Based Mechanism for Half-Metallicity and Ferromagnetism in One-Dimensional Organometallic Sandwich Molecular Wires. *J. Am. Chem. Soc.* **2008**, *130*, 13956–13960.
8. Zhou, J.; Sun, Q. Magnetism of Phthalocyanine-Based Organometallic Single Porous Sheet. *J. Am. Chem. Soc.* **2011**, *133*, 15113–15119.
9. Heber, J. Enter The Oxides. *Nature* **2009**, *459*, 28–30.
10. Mannhart, J.; Schlom, D. G. Oxide Interfaces-An Opportunity for Electronics. *Science* **2010**, *327*, 1607–1611.
11. Takagi, H.; Hwang, H. Y. An Emergent Change of Phase for Electronics. *Science* **2010**, *327*, 1601–1602.
12. Ohtomo, A.; Hwang, H. Y. A High-Mobility Electron Gas at $LaAlO_3/SrTiO_3$ Heterointerface. *Nature* **2004**, *427*, 423–426.
13. Thiel, S.; Hammerl, G.; Schmehl, A.; Schneider, C. W.; Mannhart, J. Tunable Quasi-Two-Dimensional Electron Gases in Oxide Heterostructures. *Science* **2006**, *313*, 1942–1945.
14. Xie, Y.; Bell, C.; Yajima, T.; Hikita, Y.; Hwang, H. H. Charge Writing at the $LaAlO_3/SrTiO_3$ Surface. *Nano Lett.* **2010**, *10*, 2588–2591.
15. Li, L.; Richter, C.; Paetel, S.; Kopp, T.; Mannhart, J.; Ashoori, R. C. Very Large Capacitance Enhancement in A Two-Dimensional Electron System. *Science* **2011**, *332*, 825–828.
16. Yajima, T.; Hikita, Y.; Hwang, H. Y. A Heteroepitaxial Perovskite Metal-Base Transistor. *Nat. Mater.* **2011**, *10*, 198–201.
17. Chen, H. H.; Kolpak, A. M.; Ismail-Beigi, S. Electronic and Magnetic Properties of $SrTiO_3/LaAlO_3$ Interface from First Principles. *Adv. Mater.* **2010**, *22*, 2881–2899.
18. Rondinelli, J. M.; Stengel, M.; Spaldin, N. A. Carrier-Mediated Magnetoelectricity in Complex Oxide Heterostructures. *Nat. Nanotechnol.* **2007**, *3*, 46–50.
19. Duan, C. -G.; Velev, J. P.; Sabirianov, R. F.; Zhu, Z.; Chu, J.; Jaswal, S. S.; Tsymbal, E. Y. Surface Magnetoelectric Effect in Ferromagnetic Metal Films. *Phys. Rev. Lett.* **2008**, *101*, 137208–137211.
20. Cai, T. Y.; Ju, S.; Lee, J.; Sai, N.; Demkov, A. A.; Niu, Q.; Li, Z.; Shi, J.; Wang, E. G. Magnetoelectric Coupling and Electric

Control of Magnetization in Ferromagnet/Ferroelectric/Normal-Metal Superlattices. *Phys. Rev. B* **2009**, *80*, 140415(R).
21. Jang, H. W.; Felker, D. A.; Bark, C. W.; Wang, Y.; Niranjan, M. K.; Nelson, C. T.; Zhang, Y.; Su, D.; Folkman, C. M.; Baek, S. H.; *et al*. Metallic and Insulating Oxide Interfaces Controlled by Electronic Correlations. *Science* **2011**, *331*, 886–889.
22. Lin, C. W.; Millis, A. J. Theory of Manganite Superlattices. *Phys. Rev. B* **2008**, *78*, 184405.
23. Dong, S.; Yu., R.; Yunoki, S.; Alvarez, G.; Liu, J. M.; Dagotto, E. Magnetism, Conducitivity, and Orbital Order in $(LaMnO_3)_{2n}$/$(SrMnO_3)_n$ Superlattices. *Phys. Rev. B* **2008**, *78*, 201102.
24. Nanda, B. R. K.; Satpathy, S. Spin-Polarized Two-Dimensional Electron Gas at Oxide Interface. *Phys. Rev. Lett.* **2008**, *101*, 127201.
25. Nanda, B. R. K.; Satpathy, S. Electronic and Magnetic Structure of the $(LaMnO_3)_{2n}$/$(SrMnO_3)_n$ Superlattices. *Phys. Rev. B* **2009**, *79*, 054428.
26. Nanda, B. R. K.; Satpathy, S. Polar Catastrophe, Electron Leakage, and Magnetic Ordering at the $LaMnO_3$/$SrMnO_3$ Interface. *Phys. Rev. B* **2010**, *81*, 224408.
27. Smadici, S.; Abbamonte, P.; Bhattahcarya, A.; Zhai, X. F.; Jiang, B.; Rusydi, A.; Eckstein, J. N.; Bader, S. D.; Zuo, J. M. Electronic Reconstruction at $SrMnO_3$−$LaMnO_3$ Superlattice Interfaces. *Phys. Rev. Lett.* **2007**, *99*, 196404.
28. Bhattacharya, A.; May, S. J.; te Velthuis, S. G. E.; Warusawithana, M.; Zhai, X. F.; Jiang, B.; Zuo, J. M.; Fitzsimmons, M. R.; Bader, S. D.; Eckstein, J. N. Metal-Insulator Transition and Its Relation to Magnetic Structure in $(LaMnO_3)_{2n}$/$(SrMnO_3)_n$. *Phys. Rev. Lett.* **2008**, *100*, 257203.
29. Koida, T.; Lippmaa, M.; Fukumura, T.; Itaka, K.; Matsumoto, Y.; Kawasaki, M.; Koinuma, H. Effect of A-Site Cation Ordering on the Magnetielectric Properties in $(LaMnO_3)_m$/$(SrMnO_3)_m$ Artificial Superlattices. *Phys. Rev. B* **2002**, *66*, 144418.
30. May, S. J.; Shah, A. B.; te Velthuis, S. G. E.; Fitzsimmons, M. R.; Zuo, J. M.; Zhai, X. F.; Eckstein, J. N.; Bader, S. D.; Bhattacharya, A. Magnetically Asymmetric Interfaces in a $LaMnO_3$/$SrMnO_3$ Superlattice Due to Structural Asymmetries. *Phys. Rev. B* **2008**, *77*, 174409.
31. May, S. J.; Ryan, P. J.; Robertson, J. L.; Kim, J. -W.; Santos, T. S.; Karapetrova, E.; Zarestky, J. L.; Zhai, X.; te Velthuis, S. G. E.; Eckstein, J. N.; *et al*. Enhanced Ordering Temperatures in Antiferromagnetic Manganite Superlattices. *Nat. Mater.* **2009**, *8*, 892–897.
32. Perucchi, A.; Baldassarre, L.; Nucara, A.; Calvani, P.; Adamo, C.; Schlom, D. G.; Orgiani, P.; Maritato, L.; Lupi, S. Optical Properties of $(SrMnO_3)_n$/$(LaMnO_3)_{2n}$ Superlattices: An Insulator-to-Metal Transition Observed in the Absence of Disorder. *Nano Lett.* **2010**, *10*, 4819–4823.
33. Nakamura, M.; Okuyama, D.; Lee, J. S.; Arima, T.; Wakabayashi, Y.; Kumai, R.; Kawasaki, M.; Tokura, Y. Magnetically Tunable Metal-Insulator Superlattices. *Adv. Mater.* **2009**, *21*, 1–5.
34. Kourkoutis, L. F.; Song, J. H.; Hwang, H. Y.; Muller, D. A. Microscopic Origins for Stabilizing Room-Temperature Ferromagnetism in Ultrathin Manganite Layers. *Proc. Natl. Acad. Sci. U.S.A.* **2010**, *107*, 11682–11685.
35. Sadoc, A.; Mercey, B.; Simon, C.; Grebille, D.; Prellier, W.; Lepetit, M. B. Large Increase of the Curie Temperature by Orbital Ordering Control. *Phys. Rev. Lett.* **2010**, *104*, 046804.
36. Zhai, X.; Mohapatra, C. S.; Shah, A. B.; Zuo, J. -M.; Eckstein, J. N. New Optical Absorption Bands in Atomic-Layer Superlattices. *Adv. Mater.* **2010**, *22*, 1136–1139.
37. Shah, A. B.; Ramasse, Q. M.; Zhai, X.; Wen, J. G.; May, S. J.; Petrov, I.; Bhattacharya, A.; Abbamonte, P.; Eckstein, J. N.; Zuo, J. -M. Probing Interfacial Electronic Structures in Atomic Layer $LaMnO_3$ and $SrTiO_3$ Superlattices. *Adv. Mater.* **2010**, *22*, 1156–1160.
38. Garcia-Barriocanal, J.; Cezar, J. C.; Bruno, F. Y.; Thakur, P.; Brookes, N. B.; Utfeld, C.; Rivera-Calzada, A.; Giblin, S. R.; Taylor, J. W.; Duffy, J. A.; *et al*. Spin and Orbital Ti Magnetism at $LaMnO_3$/$SrTiO_3$ Interfaces. *Nat. Commun.* **2010**, *1*, 1080.
39. Garcia-Barriocanal, J.; Bruno, F. Y.; Rivera-Calzada, A.; Sefrioui, Z.; Nemes, N. M.; Garcia-Hernndez, M.; Rubio-Zuazo, J.; Castro, G. R.; Varela, M.; Pennycook, S. J.; *et al*. "Charge Leakage" at $LaMnO_3$/$SrTiO_3$ Interfaces. *Adv. Mater.* **2010**, *22*, 627–632.
40. Wang, Y.; Niranjan, M. K.; Burton, J. D.; An, J. M.; Belashchenko, K. D.; Tsymbal, E. Y. Prediction of A Spin-Polarized Two-Dimensional Electron Gas at the $LaAlO_3$/EuO (001) Interface. *Phys. Rev. B* **2009**, *79*, 212408.
41. Lee, J.; Sai, N.; Demkov, A. A. Spin-Polarized Two-Dimensional Electron Gas through Electrostatic Doping in $LaAlO_3$/EuO Heterostructures. *Phys. Rev. B* **2010**, *82*, 235305.
42. Burton, J. D.; Tsymbal, E. Y. Highly Spin-Polarized Conducting State at the Interface between Nonmagnetic Band Insulators: $LaAlO_3$/FeS_2 (001). *Phys. Rev. Lett.* **2011**, *107*, 16601.
43. Ahn, C. H.; Bhattacharya, A.; Di Ventra, M.; Eckstein, J. N.; Frisbie, C. D.; Gershenson, M. E.; Goldman, A. M.; Inoue, I. H.; Mannhart, J.; Millis, A. J.; *et al*. Electrostatic Modification of Novel Materials. *Rev. Mod. Phys.* **2006**, *78*, 1185–1212.
44. Salamon, M. B.; Jaime, M. The Physics of Manganites: Structure and Transport. *Rev. Mod. Phys.* **2001**, *73*, 583–628.
45. Dagotto, E. Colossal Magnetoresistant Materials: The Key Role of Phase Separation. *Phys. Rep.* **2001**, *344*, 1–153.
46. Tokura, Y. Critical Features of Colossal Magnetoresistive Manganites. *Rep. Prog. Phys.* **2006**, *69*, 797–851.
47. Zener, C. Interaction between the d-Shells in the Transition Metals. II. Ferromagnetic Compounds of Manganese with Perovskite Structure. *Phys. Rev.* **1951**, *82*, 403–405.
48. Hou, F.; Cai, T. Y.; Ju, S.; Shen, M. R. Magnetic Reconstruction at Oxygen-Deficient $SrMnO_3$ (001) Surface: A First-Principle Investigation. *Appl. Phys. Lett.* **2011**, *99*, 192510–192512.
49. Fang, Z.; Solovyev., I. V.; Terakura, K. Phase Diagram of Tetragonal Manganites. *Phys. Rev. Lett.* **2000**, *84*, 3169–3172.
50. Rondinelli, J. M.; Spaldin, N. A. Structure and Properties of Functional Oxide Thin Films: Insights from Electronic-Structure Calculations. *Adv. Mater.* **2011**, *23*, 3363–3381.
51. Blöchl, P. E. Projector Augmented-Wave Method. *Phys. Rev. B* **1994**, *50*, 17953–17979.
52. Kresse, G.; Furthmüller, J. Efficiency of *ab-Initio* Total Energy Calculations for Metals and Semiconductors Using A Plane-Wave Basis Set. *Comput. Mater. Sci.* **1996**, *6*, 15–50.
53. Perdew, J. P.; Burke, K.; Ernzerhof, M. Generalized Gradient Approximation Made Simple. *Phys. Rev. Lett.* **1996**, *77*, 3865–3868.
54. Dudarev, S. L.; Botton, G. A.; Savrasov, S. Y.; Humphreys, C. J.; Sutton, A. P. Electron-Energy-Loss Spectra and the Structural Stability of Nickel Oxide: An LSDA+*U* Study. *Phys. Rev. B* **1998**, *57*, 1505–1509.
55. Sondena, R.; Ravindran, P.; Stolen, S.; Grande, T.; Hanfland, M. Electronic Structure and Magnetic Properties of Cubic and Hexagonal $SrMnO_3$. *Phys. Rev. B* **2006**, *74*, 144102.
56. Lee, J. H.; Rabe, K. M. Epitaxial-Strain-Induced Multiferrocitiy in $SrMnO_3$ from First Principles. *Phys. Rev. Lett.* **2010**, *104*, 207204.
57. Yin, W. G.; Volja, D.; Ku, W. Orbital Ordering in $LaMnO_3$: Electron−Electron *versus* Electron−Lattice Interface. *Phys. Rev. Lett.* **2006**, *96*, 116405.
58. Luo, W. D.; Franceschetti, A.; Varela, M.; Tao, J.; Pennycook, S. J.; Pantelides, S. T. Orbital-Occupancy *versus* Charge Ordering and the Strength of Electron Correlations in Electron-Doped $CaMnO_3$. *Phys. Rev. Lett.* **2007**, *99*, 036402.
59. Blöchl, P. E.; Jepsen, O.; Andersen, O. K. Improved Tetrahedron Method for Brillouin-Zone Integrations. *Phys. Rev. B* **1994**, *49*, 16223–16233.